RESEARCH

Cavitation and crack nucleation in thin hyperelastic adhesives

Florian Rheinschmidt · Michael Drass · Jens Schneider · Philipp L. Rosendahl

Abstract The present study investigates in the failure of adhesive bondings with structural silicone sealants. Point connectors of two circular metal adherends bonded with DOWSIL™ TSSA are subjected to tensile loading. We formulate and use a constitutive law that captures volumetric softening owing to the formation of cavities. Therein, cavitation is considered a process of elastic instability which is homogenized with a pseudo-elastic approach. Ultimate failure initiating from the free edges is predicted employing the framework of finite fracture mechanics. The concept requires both a strength-of-materials condition and a fracture mechanics condition to be satisfied simultaneously for crack nucleation. For the former, we use a novel multiaxial equivalent strain criterion. For the latter, we employ literature values of the fracture toughness of DOWSIL™ TSSA. The predicted onset of cavitation and ultimate failure loads are in good agreement with our experiments. The proposed model provides initial crack lengths that allow for the derivation of simple engineering models for both initial designs

F. Rheinschmidt (✉) · J. Schneider · P. L. Rosendahl
Institute of Structural Mechanics and Design, Technical University of Darmstadt, Franziska-Braun-Str. 3, 64287 Darmstadt, Germany
e-mail: rheinschmidt@ismd.tu-darmstadt.de

M. Drass
M&M Network-Ing UG, Lennebergstr. 40, 55124 Mainz, Germany

and proof of structural integrity while simultaneously extending the range of usability of the structural silicone compared to standardized approaches.

1 Introduction

Structural bondings employing silicone adhesives have become an important part of modern engineering. In mechanical engineering, the adhesives enable lightweight joints to be made between different materials, while in an architectural context, silicone adhesives enable civil engineers to design exceptional structures and façades. In all applications, the homogenous load transfer and the high tolerance of the sealant to large deformations of the adherends due to thermal mismatch between different materials are crucial advantages of silicone bondings. However, design with silicone adhesives is challenging. Nonlinear material behaviour requires advanced material models to account for large deformations. This results in additional work for engineers, as standard failure prediction approaches typically use either linear elastic fracture mechanics or strength-of-material approaches based on equivalent stress criteria. Neither is applicable to structural silicone adhesives.

Thin structural silicone bondings, such as the Thin Structural Silicone Adhesive, DOWSIL™ TSSA , investigated in the study, allow fully transparent bondings of glass, enabling completely new structures and façades to be constructed. In the case of these thin structural silicone bonds, strong constraints in the lateral direction of the adhesive layer result in volumetric loading of the material. Both material and failure models must account for volumetric effects. Assemblies with TSSA require a thorough understanding of the effects present. Therefore, the introduction is tripartite. Firstly, material models that account for volumetric softening due to cavitation are discussed. Secondly, an overview of different failure models is given. Thirdly, theories for the ultimate failure of component parts in the presence of stress singularities are discussed.

1.1 Material models

Addressing the effects of cavitation in structural silicone adhesives requires for sophisticated material models. These models can either be either micromechanically motivated or be based purely on empirical evaluation of experiments. Micromechanically motivated approaches can be divided into three subcategories according to Dal et al. (2018).

The first category splits the Helmholtz free energy function ψ into an isochoric ψ_{iso} and a volumetric part ψ_{vol}. This split, introduced by Flory (1961), proves to be an adequate approach for materials with large differences in their shear and bulk moduli. However, according to Ehlers and Eipper (1998) and Li et al. (2007), the classical approaches for ψ_{vol} fail om the case of large volumetric strains. The isochoric part of the Helmholtz free energy function has been extensively studied and many promising approaches have been given, e.g., Mooney (1940); Rivlin (1948); Ogden (1972); Arruda and Boyce (1993). Approaches modelling the volumetric part of the strain energy function often lack a physical basis, so that many fail to describe the asymptotic behaviour for large volumetric strains and are thus restricted to the regime of small volumetric strains.

The second category includes studies that analytically investigate the kinematics of single- or multi-voided macroscopic continua. A first approach was introduced by Ball (1982), where a cavity nucleates as an elastic instability at the center of a sphere composed of an incompressible matrix in n-dimensional space. The onset of instable and elastic caviation growth, the so-called bifurcation point, is calculated for the case of a Neo-Hookian material and $n = 2$ and agrees well with the results of several experiments. Stuart (1985) extended the approach of Ball (1982) to compressible matrix materials with multiple strain energy density functions, using the shooting method to determine whether cavitation occurs. Horgan and Abeyaratne (1986) studied elastic and compressible cylinders under radial loading with pre-existing voids. These studies do not introduce irreversible fracture or damage to the material. However, this approach is limited to homogeneous hydrostatic loading. The constitutive behaviour of the voided material is not accessible by these approaches, nor is the effect of a significant softening of the material after the onset of cavitation.

The third category uses homogenization techniques, where a given initial void fraction is present in an otherwise incompressible material. Danielsson et al. (2004) based a study on the results of Hou and Abeyaratne (1992). Homogenized Helmholtz energy funcions were developed to represent poro–hyperelastic material behaviour. Li et al. Li et al. (2007, 2008) followed a similar approach as Danielsson et al. (2004), but used a Voigt-type homogenization technique and obtained a compressible constitutive law accounting for cavitation and cavitation growth. Further studies using the same approach were carried out by Dal et al. (2013) and Timmel et al. (2007). However, large volumetric strains were not discussed in the above mentioned studies, although they are critical in the design of structural silicone bondings that undergo large deflections during loading. For example, TSSA is commonly applied in the form of penny-shaped bondings where small axial displacements result in large volumetric strains in the center of the adhesive layer (Drass and Schneider 2016).

(Drass and Schneider 2016; Drass et al. 2018a, b, c, 2019) have extensively studied the behavior of TSSA, focussing in particular on large volumetric strains. Figure 1 shows the stress whitening effect of DOWSIL™ TSSA for tensile tests on a penny-shaped specimen. The whitening effect shown results from an initial void fraction detected with CT measurements and transmission electrons microscopy (Drass et al. 2019). These initial voids expand elastically under volumetric loading and result in a softening of the material. This is an important distinction to other rubber-

like materials investigated, e.g., by Gent and Lindley (1959), Ball (1982), Hou and Abeyaratne (1992) or Lopez-Pamies et al. (2011a, b). While the above studies focussed either on a defect free material or zero-dimensional defects of arbitrary shape, the present study accounts for a finite porosity inherent to the material and prior to loading. This can be observed in the stress whitening that occurs during tensile tests of penny-shaped specimens. While in the above studies, a small to medium number of macroscopic cavities occur, TSSA shows a very large number of microscopic cavities. Alongside the disappearance of the whitening when unloading the material, this results in the conclusion, that the growth of cavities in TSSA is purely elastic, Drass et al. (2019). Additional support for this hypothesis comes from cyclic tests performed on penny–shaped specimens under tensile loading (Drass et al. 2020). Here, the classical Mullins effect for isochoric loading is identified alongside an extended Mullins effect that occurs under volumetric deformations. For cyclically loaded penny–shaped specimens, unloading and reloading path are not equal. However, for each reloading step, the initial stiffness resumes the initial value of the virgin material, so that macroscopic damage in the material resulting from inelastic cavitation growth can be neglected. A micromechanically motivated constitutive model that captures the softening of the material after the onset of cavitation was developed based on extended Nelder polynomials (Nelder 1966). The combination of this novel Helmholtz energy function with arbitrary isochoric strain energy functions allows the representation of either purely isotropic or purely volumetric load cases. In order to adequately represent the general constitutive behavior of TSSA under arbitrary monotonic deformations, Drass et al. (2020) introduced an additional term to the Helmholtz free energy function, using methods based on the concept of pseudo-elasticity introduced by Lazopoulos and Ogden (1998). Additionally, a study focussing on the cyclic loading and Mullins-effect related mechanisms present in TSSA was conducted by Drass et al. (2020). A numerical implementation of both monotonic and cyclic loading is available for commercial FE-software Ansys as an UserHyper-subroutine. However, as a first approach on the crack nucleation in poro-hyperelastic materials subject to cavitation, the present study only regards the monotonic case.

Fig. 1 Effect of stress whitening in DOWSIL™ TSSA under volumetric loading during experiments

This approaches are applicable to both large and small volumetric and isochoric deformations. Cavitation is described as a purely elastic process resulting from initial pores within the material and in good agreement with previous studies. To evaluate the failure of point connectors under quasi-static loading, both a failure criterion for the material and a theoretical framework for ultimate failure prediction of elastomers are required.

1.2 Bulk failure models

Normative approaches such as the European Technical Approval Guideline (ETAG-002) require a minimum adhesive layer thickness of 4 mm and a height to width ratio between 1 : 1 and 1 : 3. The reason for this strict adhesive design rule is the danger of cavitation in thin and slender adhesive layers due to the strong lateral constraints.

In addition to the accurate description of the constitutive behavior, the prediction of crack nucleation and subsequent ultimate failure requires adequate failure models. These failure models must be capable of representing the material's strength and ultimate extensibility under arbitrary and multiaxial loading. Complex stress, stretch, or strain states that the material can withstand indefinitely, define the so-called safe region. This region is bounded by a failure surface, that defines the stress, stretch, or strain state at which the material fails (Kolupaev 2018). In the case of silicones with a finite porosity and a distinct regime of possible volumetric deformations, two separate failure modes can be identified. The failure modes are distinguished into dilatational or distortional failure modes as outlined

by Blatz (1963) or Lindsey (1967). In the context of finite porosity silicones, dilatational or volumetric failure corresponds to the initial onset of cavitation growth in the material at the bifurcation point. Distortional failure corresponds to deformations that leave the volume of the material unchanged.

Initial pioneering work on the dilatational failure was done by Busse (1938), Yerzley (1939) and Gent and Lindley (1959). There, a yield point in the load displacement behavior was experimentally identified for rubber cylinders bonded to metal adherends and subjected to tensile loading. From this yield point, cavitation growth occurs. Further experimental work based on these experiments was carried out by Lindsey (1967), who replaced the metal adherends with transparent ones made of poly-methyl methacrylate. This setup, in combination with transparent silicones, allows for optical tracking of individual cavities. The result of this experimental design was a critical hydrostatic load at which cavities begin to grow. This so-called bifurcation point was found to be related to the initial shear modulus μ of the bulk material with the critical Piola–stress $P_{cr} = 5/2\mu$. The initial shear modulus is here related to initial gradient of the shear stress–strain relation of the material and related in Neo-Hookean materials to the C_{10} parameter. In terms of models for predicting dilatational failure, (Hou and Abeyaratne 1992) developed a cavitation criterion by applying a variational approach to arbitrary deformation states. This criterion allows one to predict the onset of cavitation in incompressible media and agrees well with the above mentioned experiments.

Early studies of the distortional failure surface of rubber-like silicones under multiaxial loading used classical stress-based failure surfaces known from metals to describe the failure surface (Sharma and Lim 1965; Jones and Kruse 1966; Sharma 1966; Knauss 1967; Dickie and Smith 1969; Smith and Rinde 1969; Tschoegl 1971; Kawabata 1973). However, this approach has not been found to be well suited to the properties of silicones and is not capable of describing the failure surfaces. In addition, the identification of failure loads in terms of stresses is challenging since these are not directly accessible from the experimental data. Recent approaches have therefore used polynomial (Hamdi et al. 2006, 2007) or exponential (Hamdi and Mahjoubi 2015) functions to describe the test data measured in principal stretch space. The results of these studies were promising and the experimental results

were well represented. Staudt et al. (2018) reformulated the results of Hamdi et al. (2006), Hamdi and Mahjoubi (2015) in terms of strain space. However, all of the above mentioned studies were limited to one or a few polymers and were not able to provide the failure surface for arbitrary silicones.

Compared to early studies on failure surfaces, significant mathematical progress has been made, e.g., by Altenbach et al. (2018), Kolupaev (2018), or Rosendahl et al. (2019), who generalized the classical failure criteria of von Mises, Drucker-Prager, Tresca, Mohr-Coulomb or Rankine. Altenbach et al. (2018) and Podgórski (1985) provided two parametric shape functions that combine several of the above classical shapes forms of failure surfaces. Of these, Podgórski (1985) is able to represent all the classical shapes of the failure surface while providing a differentiable and strictly convex mathematical formulation, cf. Kolupaev (2018), Rosendahl et al. (2019). The bulk failure behavior of TSSA is extensively studied by Drass et al. (2018c) and both the shape parameters and the equivalent stretches are determined by Rosendahl et al. (2019). Combined with the advanced constitutive models, this bulk material failure model allows for the presence of cavities and predicts failure not at the point of bifurcation, but at the point of total rupture of the bulk material.

1.3 Notch-induced crack formation

The failure models discussed above apply in the absence of stress raisers. That is, when a homogenous, uniaxial or multiaxial loading is present. In the case of notches or bimaterial interfaces with their complex load distributions, the local evaluation of equivalent stress, strain or stretch criteria regularly underestimates the durability of the structures. Therefore, studies that focus on the ultimate failure of structures often do not use the strength-of-material based concept of local equivalent stress or stretch, but instead use non-local approaches. Therefore, equivalent failure criteria are not evaluated directly at the stress raiser, but at a fixed distance. The derivation of the distance depends on the material. Taylor (2008) developed the theory of critical distances where the length scale is derived from the linear-elastic material parameters. This length scale is then used directly by the point method (PM) or by the line method (LM), where equivalent stresses

are calculated either pointwise at the derived distance from the stress concentration or averaged over this derived length. The derivation of this intrinsic length scale by the theory of critical distances according to Taylor (2008) fails, if no explicit Young's modulus can be given, as is the case for hyperelastic materials. For rubber-like materials, Ayatollahi et al. (2016) and Heydari-Meybodi et al. (2017) applied a stretch criterion at a certain distance from notches. The results of these studies were good, but not generalizable. Other approaches to the failure stresses of hyperelastic materials either compare the averaged strain energy density in the vicinity of notches to a certain threshold (Berto 2015; Heydari-Meybodi et al. 2018) or use phase field models (Miehe and Schänzel 2014). Both of these approaches can describe experimental results, but are dependent on either the distance to the notch or the regularization length in the case of the phase field. Pipes et al. (1979) showed a relationship between length parameters and the geometry so that the length scales cannot be considered as a material constant.

Another approach to evaluating the failure of a given structure is based on energetic considerations rather than material strength. Griffith (1921), a pioneer in fracture mechanics, postulated that a certain amount of energy per unit crack surface area is required at the microscopic level to drive crack extension. However, this approach was limited to brittle bodies with pre-existing cracks. Although the fracture mechanics approach has been adapted to compliant and rubber-like materials in the form of a critical tearing energy (Rivlin and Thomas 1953; Thomas 1955, 1958), a local evaluation of the energy criterion also fails at weak stress singularities, such as bimaterial interfaces. That is, why e.g. Lake and Thomas A.G. (1967) and Lake (1995) introduce a length scale with a diameter at the crack tip as stress raisers to predict the onset of a tearing in the material. This then registers as a nonlocal approach as well. The determination of the length scales ideally requires a physically sound derivation applicable to large deformations and nonlinear materials.

Hashin (1996) introduced the idea of Finite Fracture Mechanics (FFM), where an initial crack length is derived from physical considerations. Leguillon (2002) formalized this approach in terms of a coupled criterion where a fracture mechanical (energetic) criterion and a bulk material failure criterion must be satisfied simultaneously along the crack path. The results from this

approach are promising. It is applied to different forms of notches (Cornetti et al. 2019), open hole geometries (Weißgraeber et al. 2016; Felger et al. 2017a) and mixed-mode configurations (Talmon l'Armée et al. 2017; Felger et al. 2017b), joint failure (Stein et al. 2015; Felger et al. 2019), thermo-mechanical loading configurations (Leguillon et al. 2015), crack pattern prediction (Rosendahl et al. 2017), the occurrence of transverse cracks in cross-ply laminates (García et al. 2018, 2019), 3D crack initiation (Doitrand and Leguillon 2018), free edge delamination (Frey et al. 2021), and the assessment of natural hazards and porous and non-ideal brittle media (Rosendahl and Weißgraeber 2020a, b). Furthermore, a micromechanical explanation of the effects present is available (Leguillon et al. 2018; Souguir et al. 2020). For further applications, a review of the application for linear-elastic materials is provided by Weißgraeber et al. (2016). The good agreement with experimental data in the aforementioned studies is due to a physical sound setup where no additional assumptions on arbitrary length scales are required.

Here, the concept of large deflections is already considered. Based on this work, the present study now combines the advances in material models that account for cavitation and its softening effects with the successful failure models for combined dilatational-distortional failure to investigate the ultimate loads of thin structural bondings made of silicone. It is organized as follows: First, the theoretical background of the material model, the distortional failure surface and the coupled criterion are presented. Then, the numerical model with its boundary conditions and settings is presented. The experimental results ar also discussed. Finally, the results are presented in the form of a comparison between model and experiments. In addition, the influence of changing diameters is considered and the paper concludes with design rules for the design and proof of structural integrity.

2 Theoretical foundations

This section discusses the governing equations and models which are used to determine the ultimate loads of penny-shaped TSSA bonds. First, the pseudo-elastic model that accounts for volumetric softening is briefly introduced. Therefore, the work of Drass et al. (2020) is

summarized. There, the Finite-Element user subroutine used in this study is also given.

2.1 Constitutive behaviour accounting for volumetric softening

The pseudo-elastic material model is based on a decomposition of the Helmholtz free energy function ψ into three different parts. In addition to a volumetric part ψ_{vol}, an isochoric part ψ_{iso} and a couple term ψ_{couple} are used,

$$
\begin{aligned}
\psi\left(\boldsymbol{B}\right) = {} & \psi_{\text{iso}}\left(\bar{\boldsymbol{B}}\right) + \psi_{\text{vol}}\left(J\right) \\
& + \psi_{\text{couple}}\left(I_1^{\bar{\boldsymbol{B}}}, I_2^{\bar{\boldsymbol{B}}}, J\right).
\end{aligned}
\tag{1}
$$

Here, $\boldsymbol{B}$ denotes the left Cauchy-Green tensor with its deviatoric part $\bar{\boldsymbol{B}}$, the corresponding first two invariants $I_1^{\bar{\boldsymbol{B}}}, I_2^{\bar{\boldsymbol{B}}}$ and J being the determinant of the deformation gradient $\mathbf{F}$.

In Drass et al. (2020) the couple term ψ_{couple} $\left(I_1^{\bar{\boldsymbol{B}}}, I_2^{\bar{\boldsymbol{B}}}, J\right)$ is motivated by the need to distinguish between purely isochoric and purely volumetric deformations and, in particular, to correctly represent mixed isochoric-volumetric deformation states. In order to describe the mechanisms involved, the two limit cases of purely isochoric and purely volumetric loading are discussed first. Then, the goals of ψ_{couple} are briefly discussed. A detailed derivation and discussion of ψ_{couple} is given in Drass et al. (2020).

Purely isochoric deformations are described by the isochoric part of the Helmholtz free energy function $\psi_{\text{iso}}\left(\bar{\boldsymbol{B}}\right)$. Drass et al. (2020) found, that a simple Neo-Hookean strain energy density function adequately describes TSSA in this case,

$$
\psi_{\text{iso}}\left(I_1^{\bar{\boldsymbol{B}}}, I_2^{\bar{\boldsymbol{B}}}\right) = \frac{\mu}{2}(I_1^{\bar{\boldsymbol{B}}} - 3),
\tag{2}
$$

with the initial shear modulus μ as a material constant.

Drass et al. (2018b) showed that purely volumetric loading of TSSA can be described by Nelder polynomials (Nelder 1966), such that the volumetric term of the Helmholtz free energy function reads,

$$
\psi_{\text{vol,ND}} = \int \frac{J - 1}{\sum_{i=0}^{3} \kappa_i (J - 1)^i} \, \mathrm{d}J,
\tag{3}
$$

with the material constants κ_i, for $i \in \{0, 1, 2, 3\}$.

The couple term $\psi_{\text{couple}}\left(I_1^{\bar{\boldsymbol{B}}}, I_2^{\bar{\boldsymbol{B}}}, J\right)$ begins to govern the material behavior in the case of mixed-mode lading. Therefore, in the limit case of purely volumetric behavior, the couple term must vanish, since the expression 3 is sufficient to describe the material response. In the other limit case of purely isochoric deformations, the material is considered quasi incompressible. In order to obtain the desired behavior of the Helmholtz free energy function, an additional variable, which depends on the actual stretches, is introduced to the couple term, which is formulated directly in the stretches according to Drass et al. (2020),

$$
\psi_{\text{couple}}\left(I_1^{\bar{\boldsymbol{B}}}, I_2^{\bar{\boldsymbol{B}}}, J\right) = \tilde{\psi}_{\text{couple}}\left(\lambda_1, \lambda_2, \lambda_3\right).
\tag{4}
$$

The extensive derivation of the couple term along with a Fortran–implementation as a UserHyper-subroutine for THE COMMERCIAL FE- SOFTWARE Ansys is given in Drass et al. (2020).

2.2 Bulk failure model for hyperelastic materials

As discussed in Sect. 2, Rosendahl et al. (2019) reformulated the Podgorsky failure surface model and showed that it allows to sufficiently represent the critical states under multiaxial loading for TSSA sufficiently. In the present work, the criterion is applied in terms of stretches. The distinction between dilatational and distortional failure requires the introduction of new variables that replace the standard base system of principal stretches λ_i. Starting from the hydrostatic axis defined by $\lambda_1 = \lambda_2 = \lambda_3$, a locally perpendicular hyperbolic isosurface defined by a constant volumetric deformation is set up, $\lambda_1 \lambda_2 \lambda_3 = const$. All isochoric deformations can be represented on this isosurface. In particular, ultimate loads result in single points on this surface, so that a distortional failure surface as a distinction between safe spaces and distortional failure becomes an isoline on this surface. Describing this failure surface within the principal stretch coordinate system is challenging. A cylindrical coordinate system is introduced, with the cylindrical axis aligned with the hydrostatic axis. Therefore, distortional failure is described only in the remaining two coordinates. Before defining these variables, some invariants of the left stretch tensor $\mathbf{V}$ and its deviatoric part $\mathbf{V}_{\text{dev}} = \mathbf{V} - \text{tr}\mathbf{V}/3\,\mathbf{I}$ are introduced. $(\cdot)'$ denotes the invariants of the deviatoric left stretch tensor,

$$I_1^{\mathbf{V}} = \text{tr}\mathbf{V} = \lambda_1 + \lambda_2 + \lambda_3, \tag{5}$$

$$I_2^{\bar{V}} = \frac{1}{2}\left(\text{tr}\bar{V}^2 - (\text{tr}\bar{V})^2\right) \tag{6}$$

$$= \frac{1}{6}\left((\lambda_1 - \lambda_2)^2 + (\lambda_2 - \lambda_3)^2 + (\lambda_3 - \lambda_1)^2\right), \tag{7}$$

$$I_3^{\bar{V}} = \det\bar{V}$$

$$= \left(\lambda_1 - \frac{1}{3}I_1^{\mathbf{V}}\right)\left(\lambda_2 - \frac{1}{3}I_1^{\mathbf{V}}\right)\left(\lambda_3 - \frac{1}{3}I_1^{\mathbf{V}}\right). \tag{8}$$

Based on these invariants, so-called Haigh-Westergard coordinates can be defined, which allow the description of purely isochoric deformations with distortional failure:

$$\rho^{\mathbf{V}} = \sqrt{2I_2^{\bar{V}}}, \tag{9}$$

$$\theta^{\mathbf{V}} = \frac{1}{3}\arccos\left(\frac{3\sqrt{3}}{2}\frac{I_3^{\bar{V}}}{I_2^{\bar{V}\,3/2}}\right). \tag{10}$$

$\rho^{\mathbf{V}}$ defines the distance to the hydrostatic axis, while $\theta^{\mathbf{V}}$ is an angle, measured from the projection of a λ_1-axis onto the isosurface. However, due to the isotropy of the material and the arbitrariness of the ordering of eigenvalues in a given tensor, the angle $\theta^{\mathbf{V}}$ is limited to $[0, \pi/3]$ and describes 6 different points on the deviatoric surface.

After the introduction of these variables, the PBP failure surface for distortional bulk material failure reads

$$\lambda_{\text{eq}} = \rho^{\mathbf{V}} \cos\left(\beta\frac{\pi}{3} - \frac{1}{3}\arccos(\alpha\cos(3\theta^{\mathbf{V}}))\right), \tag{11}$$

with the two shape parameters $\alpha \in [0, 1]$ and $\beta \in [0, 1]$. The failure surface describes the isoline, where this equivalent stretch is equal to a given critical stretch,

$$\frac{\lambda_{\text{eq}}(\mathbf{V})}{\lambda_{\text{c}}} = 1. \tag{12}$$

For a more detailed derivation and description as well as an extensive overview of the development of different failure surfaces, Rosendahl et al. (2019) and Kolupaev (2018) are recommended.

2.3 Notch-induced failure model

Predicting component failure is challenging because the homogeneous strain and stress states known from material testing are generally not present. Instead, there are complex loading conditions and singular stress and strain concentrations that must be considered. The general approach of fracture mechanics is based on energetic criteria and rather than strength-of-materials criteria. Griffith (1921) proposed the concept of fracture toughness as a critical threshold for the energy stored in the vicinity of cracks. The strain energy is released by crack expansion and is considered to be stored in the surface energy of the new crack surfaces. The Griffith criterion is therefore,

$$\mathcal{G}(A) = -\frac{d\Pi}{dA} = \mathcal{G}_{\text{c}}, \tag{13}$$

as the derivative of the total potential energy Π with respect to the crack surface A. On the right hand side $\mathcal{G}_{\text{c}}$ denotes the material property of fracture toughness. In the absence of strong stress singularities, such as crack tips, the energy release rate vanishes. Especially at bimaterial interfaces, weak singularities are present, so that on the one hand the stresses and strains tend to infinity, while on the other hand the energy release rate vanishes. Thus, at the interface, the Griffith criterion cannot predict crack nucleation, while the structure would fail immediately if a strain or stress based failure criterion is evaluated locally. As a consequence, the failure loads predicted by the Griffith energy based criterion are infinitely high, while the failure loads from a strength-of-material approach tend to be zero. therefore, resolving this contradiction requires a different approach. Finite Fracture Mechanics as proposed by Hashin (1996) addresses this problem. Within this theory, both an energy criterion and a failure criterion must be satisfied simultaneously along the crack path. This approach is formalized by the coupled criterion proposed by Leguillon (2002),

$$\lambda_{\text{eq}}(\Delta A, \boldsymbol{u}_{\text{f}}) \geq \lambda_{\text{c}} \quad \wedge \quad \bar{\mathcal{G}}(\Delta A, \boldsymbol{u}_{\text{f}}) \leq \mathcal{G}_{\text{c}}. \tag{14}$$

In both these criteria, the continuously growing crack area is replaced by the incremental crack area in the argument of the equivalent stretch λ_{eq} and the incremental energy release rate $\bar{\mathcal{G}}$. In addition, the energy release rate introduced by Griffith (1921) is replaced

by an incremental energy release rate $\bar{\mathcal{G}}$ defined by

$$\bar{\mathcal{G}}(\Delta A, \boldsymbol{u}) = \frac{1}{\Delta A} \int_{\Delta A} \mathcal{G}(A, \boldsymbol{u}) \mathrm{d}A = -\frac{\Delta \Pi}{\Delta A}. \quad (15)$$

This expression describes the energy released by an instantaneous crack formation of a given finite length ΔA at an applied deformation $\boldsymbol{u}$. The physical interpretation of the coupled criterion as written in Eq. 14 is crucial to understanding the advantages of the Finite Fracture Mechanics over classical nonlocal approaches. If both the equivalent stretch criterion and the modified energy criterion, which takes into account the initial nucleation of finite size cracks, are satisfied over the entire finite crack area ΔA, then the coupled criterion is satisfied and instantaneous nucleation of a finite-sized crack is predicted. In contradiction to nonlocal approaches no additional crack length is introduced. Instead, this length scale is derived from the coupling of the two fundamental criteria. The presence of finite size cracks thus results in an additional variable that is to be determined. While both classical criteria predict a failure displacement u_f, in the case of FFM the critical crack length ΔA has to be determined additionally from Eq. 14.

The criteria used to define the overload the material in the context of the present work is based on stretch rather than stress as originally proposed by Leguillon. Since the stretch criteria outlined above can adequately describe the strength of TSSA, only the fracture toughness of TSSA needs to be determined. Therefore, the work of Rheinschmidt et al. (2023) is considered, where both mode I and mode III are determined. From these material parameters, the ultimate loads of structures can be derived without further assumptions about internal length or initial cracks. To apply Finite Fracture Mechanics to penny-shaped joint made of TSSA, a finite element model is set up in Ansys.

3 Numerical evaluation of Finite Fracture Mechanics

Stretches and incremental energy release rates are calculated using Ansys commercial finite element analysis (FEA) software. The penny–shaped point fasteners of interest in this study, with an adhesive thickness of 1 mm, are rotationally symmetric. Taking advantage of this property, a two–dimensional FE–model is built

Table 1 Material parameters for TSSA for the pseudo-elastic cavitation model obtained from Drass et al. (2020)

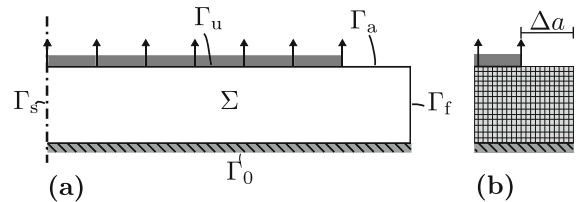| Parameter	Value
μ	2.6652 MPa
κ_0	0.0004 MPa^{-1}
κ_1	0.2699 MPa^{-1}
κ_2	0.2501 MPa^{-1}
κ_3	-0.1950 MPa^{-1}

Fig. 2 Depiction of finite element model with **a** the boundary value problem and **b** the mesh along the crack path

from axially symmetric elements. Cavitation and the resulting softening of the material are considered using the USERHYPER-subroutine as described by Drass et al. (2020). The parameters for the material model are given in Table 1. Figure 2 shows the problem domain and the discretization near the free edge. Preliminary experiments showed that cracks nucleate as a cohesive crack within the bulk material. The failure region is located at a distance of approximately 20 % of the radius from the outer edge of the specimen. The theory of Finite Fracture Mechanics demands for a stress concentration, e.g. at the free edge of the bi-material interface. The determined crack length from the present study provides a mean of evaluating the agreement between our virtual testing approach and experiments. To this end, we assume that the crack nucleates with a finite length Δa from the free edge parallel to the bi-material interface as a cohesive failure of the bulk material. Cohesive failure can be modelled using the fracture properties of the bulk material and the failure criterion, even though the numerical model geometrically indicates adhesive failure. This, combined with the strong elastic contrast between the adhesive and the adherend, allows the adherend to be modelled by vanishing radial displacements and tangential rotations along the interfaces. Cracks are implemented by locally removing this displacement boundary condition. With the determined initial crack length Δa, a failure region is obtained,
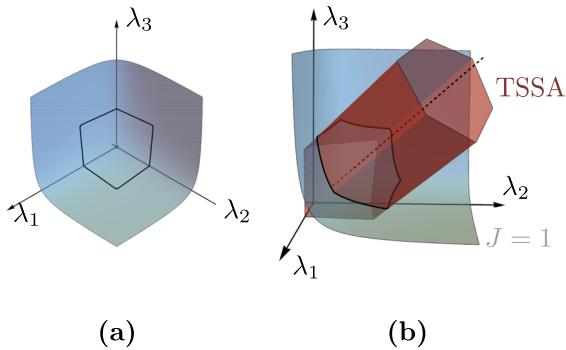
Fig. 3 Equivalent failure criterion in stretch space: **a** projection onto te isosurface of isochoric deformations and **b** with the intersection of the deviatoric failure criterion in red with the isosurface of isochoric deformation in grey. The dashed line denotes the hydrostatic axis

marking the area of the penny–shaped fastener, where the point connector fails initially.

The boundary value problem to be solved is now given by

$$
\begin{cases}
-\operatorname{div}\boldsymbol{\sigma} = 0 & \text{in } \Sigma, \\
\boldsymbol{u} = 0 & \text{along } \Gamma_0, \\
\boldsymbol{u} = \boldsymbol{u}^* & \text{along } \Gamma_{\mathrm{u}}, \\
\boldsymbol{u} = \boldsymbol{u}_{\mathrm{symm}} & \text{along } \Gamma_{\mathrm{s}}, \\
\boldsymbol{\sigma}\cdot\boldsymbol{n} = 0 & \text{along } \Gamma_{\mathrm{f}}\cup\Gamma_{\mathrm{a}},
\end{cases}
\tag{16}
$$

where $\boldsymbol{\sigma}$ denotes the Cauchy stress tensor, $\boldsymbol{u}$ the displacement field vector, $\boldsymbol{n}$ the unit outward facing normal vector and $\delta\Sigma = \Gamma_{\mathrm{f}}\cup\Gamma_{\mathrm{u}}\cup\Gamma_{\mathrm{s}}\cup\Gamma_0\cup\Gamma_{\mathrm{a}}$ the boundary of the problem domain Σ. Along the outer boundary Γ_{f} a stress-free boundary condition is imposed, while the boundary condition along the rotation axis Γ_{s} represents the symmetry propertyin this region. In particular, neither displacement in radial direction nor nodal rotation around a tangential axis along the central axis is allowed. The rigid adherent at Γ_0 is represented by clamping the bottom edge with vanishing displacements. Loading is induced at the upper adherent Γ_{u} by a prescribed uniform displacement $\boldsymbol{u}^*$ in axial direction with vanishing displacements in radial direction and vanishing rotation around the tangential axis. Cracks are represented by stress-free boundary conditions along Γ_{a}. Quadratic displacement functions are used to adequately represent displacements and stresses.

Due to the complex material model (Drass et al. 2020), an external displacement of 1.5 mm is induced in 2000 increments to ensure sufficient numerical sta-

bility. Along the crack path, the mesh consists of uniform quadratic shaped elements with an edge length of 0.0625mm each. While stretches needed to evaluate the equivalent stretch criterion are evaluated in the uncracked configuration with $\Delta a = 0$, the calculation of the incremental energy release rate has a higher numerical cost. In the present study, the energy release rate is computed from the difference of the strain energies in the cracked and uncracked configurations. To do this, 25 different boundary value problems are solved for each configuration studied, with the crack length varying between 0.0625 mm to 1.5 mm. To avoid mesh dependencies of the potential energies, both the uncracked and all cracked configurations are computed using the same discretization. The energy release rate is then calculated from the strain energy of the uncracked configuration,

$$
\Pi_0^i = \Pi_0^i(u),
\tag{17}
$$

and the strain energy of the cracked configuration dependent on the crack length of the configuration,

$$
\Pi_1^i = \Pi_1^i(u, \Delta a).
\tag{18}
$$

In total, the difference in potential energies is now related to the crack surface created, such that the incremental energy release rate as a function of both external displacement and initial crack length is given by

$$
\bar{\mathcal{G}}(u, \Delta a) = -\frac{\Pi_1^i(u, \Delta a) - \Pi_0^i(u)}{2\pi r\,\Delta a - \Delta a^2},
\tag{19}
$$

where r denotes the specimens radius. In general, cracks in adhesives are not subject to a single mode of failure. Instead, crack initiation must be considered as a mixed-mode problem. It is difficult to separate the energy released into the different failure modes. In addition, there are no fracture toughness measurements of mode II for DOWSIL™ TSSA. However, Rheinschmidt et al. (2023) determined both mode I and mode III fracture toughness based on differently loaded double cantilever beam specimen. The experiments indicate a mode III fracture toughness approximately two times the value of mode I fracture toughness $\mathcal{G}_{\mathrm{Ic}}$. Considering the typically higher fracture toughness under mode II loading compared to mode I, $\mathcal{G}_{\mathrm{IIc}} > \mathcal{G}_{\mathrm{Ic}}$, the assumption of $\mathcal{G}_{\mathrm{c}} = \mathcal{G}_{\mathrm{Ic}}$ results in a conservative model.

There are two ways to evaluate the strength criterion. On the one hand, the crack path can be labeled overloaded if the equivalent stretch at each point along the crack path exceeds the critical threshold λ_c. This is known as the point method. On the other hand, the equivalent stretch averaged over the entire potential crack path $\bar{\lambda}_{eq}(\Delta a)$ must exceed the critical threshold λ_c,

$$\bar{\lambda}_{eq}(u, \Delta a) = \frac{1}{\Delta a} \int_0^{\Delta a} \lambda_{eq}(u, x) dx = \lambda_c. \qquad (20)$$

The latter procedure is called the line method (Taylor 2008). Due to the good results observed by Rosendahl et al. (2018, 2019) when applying the line method to silicone adhesives, the current study also follows this approach.

3.1 Generation of the optimization problem

Specimens with diameters of $d = 40\,mm$ and $d = 50\,mm$ are set up numerically and compared with experimental results. Both the incremental energy release rate, Eq. 19 and the equivalent stretch, Eq. 20, are used to evaluate the crack initiation as described in Eq. 14 . The critical load is now defined by the minimum external displacement u_f for which the coupled criterion holds. This leads to the optimization problem,

$$u_f = \min_{u, \Delta a} (u \mid u > 0, \ \exists \Delta a > 0 :$$
$$\bar{\lambda}_{eq}(u, \Delta a) \geq \lambda_c \wedge \bar{\mathcal{G}}(u, \Delta a) \geq \mathcal{G}_c), \quad (21)$$

which is solved by the said critical displacement u_c and a corresponding crack length Δa. The optimization problem is solved with λ_{eq} and $\bar{\mathcal{G}}$ interpolated by bicubic splines in the commercial mathematical toolkit WOLFRAM MATHEMATICA. The critical stretch λ_c along with the two shape parameters α and β are given in Table 2. The fracture toughness for TSSA is also given there.

3.2 Experimental data

In order to validate the results of from the numerical failure predictions, experiments were performed by Hagl et al. (2012a, b), Santarsiero et al. (2017), Drass et al. (2020). A detailed discussion of the experimental

Table 2 Parameters for the equivalent stretch criterion of DOWSIL™ TSSA with the shape parameters α and β and the critical stretch λ_c. The values are obtained from Rosendahl et al. (2019). The fracture toughness $\mathcal{G}_c$ is obtained from Rheinschmidt et al. (2023)

Parameter	Value
α	0.9999
β	0.8175
λ_c	1.64 ± 0.15
$\mathcal{G}_c$	3.83 ± 0.79

setup is given there. Only a compact overview is given here. The specimens are made of two steel cylinders that are bonded by a thin layer of DOWSIL™ TSSA with a nominal thickness of $1\,mm$. The experimentally tested specimens with diameters $d = 40\,mm$ and $50\,mm$ are cured in an autoclave according to the specifications of Sitte et al. (2011). After fabrication, the specimens are loaded with uniaxially at a loading rate of 0.1mm/min. Deformations are obtained from a DIC system. For this purpose, the specimen is coated with whitener and then a black speckle pattern is applied. Figure 4 shows a tested specimen with whitener, speckle pattern and the whitening effect in the TSSA as well as the experimental setup with the stereo camera system. From the experiments, both information on the constitutive behavior in from of reaction forces and displacements and the failure loads in terms of both critical reaction force and axial displacement, are derived.

Failure of the test specimen begins in an area approximately at about $0.2 \times r$ measured from the outer edge of the specimen. Then it propagated unstably throughout the specimen.

4 Results

Figure 5 shows the experimentally determined failure loads in a reaction force-displacement diagram. Experimental test data are represented by dashed lines. Solid lines represent the numerically calculated results of this study. The reduction in stiffness of the material due to the growing cavities does not lead to a fatal cracking and ultimate failure of the material. Therefore, cavitation cannot be considered as a material failure. Instead, an elastic instability occurs and cavities grow, greatly
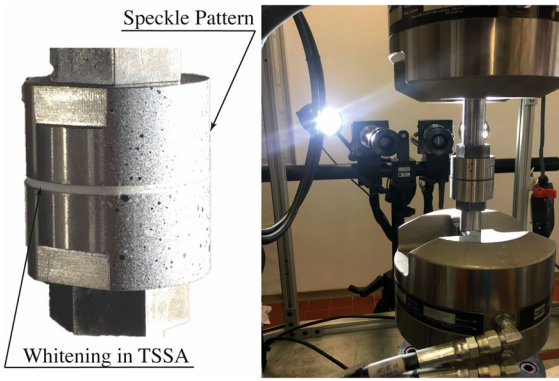
Fig. 4 Pancake test specimen with whitening effect and experimental setup with the digital image correlation system

Table 3 Tabular values of the experimentally and numerically determined failure loads in terms of critical displacements u_c and critical forces F_c

	$\varnothing = 40$ mm	$\varnothing = 50$ mm
u_c^{exp}	1.28 ± 0.15 mm	1.18 ± 0.11 mm
F_c^{exp}	6904 ± 414 N	10823 ± 415 N
u_c^{num}	1.35 ± 0.11 mm	1.35 ± 0.11 mm
F_c^{num}	7465^{+686}_{-528} N	11561^{+1085}_{-826} N
Δa^{num}	$\mathbf{1.099 \pm 0.25}$ mm	$\mathbf{1.10 \pm 0.26}$ mm

Numerical results in the brackets account for the results of the optimization problem in Eq. (21) considering the uncertainties in λ_c and $\mathcal{G}_c$ as given in Table 2. Additionally, the initial crack lnegth as a result of the optimization problem (21) are given

reducing the ability of the material to transfer loads. The present pseudo-elastic material model is able to represent this softening well. In particular, the bifurcation point is well represented as the critical displacement at which cavitation begins and the material begins to whiten. Marked by a square are the ultimate failure points of the experimental and numerical setups. The critical failure loads in terms of displacements and reaction forces are given in the Table 3. The experimental results are shown with the determined uncertainties. The error bars in Fig. 5 show one standard deviation. In the case of numerically determined failure data, Table 3 gives the results of the optimization problem, Equation (21), taking into account the uncertainty in TSSA strength λ_c and fracture toughness $\mathcal{G}_c$, see Table 2. To quantify these uncertainties, 1000 pairs of $(\lambda_c, \mathcal{G}_c)$ are generated by the Mathematica Random number generator. The optimization problem (21) is solved for each

pair individually. From these values for u_c and Δa, the mean value of critical displacements and associated initial crack lengths are derived. The error bars in vertical direction show the reaction force calculated from the Ansys model, taking into account one standard deviation of the critical displacements.

It should be noted that FFM overestimates the critical failure loads. In the case of a 40 mm radius, the numerical results are within a 95% confident interval of the experimental results, while in the case of the larger diameter the deviation between the predicted displacements and the experimental failure loads is larger than the standard deviation of the experiments. However, the confidence intervals overlap. Overestimation of failure loads using FFM is a known phenomenon cf. Rosendahl et al. (2018, 2019). Additionally, the determined initial crack length Δa^{num} lies between 5.4 and 3.4% of the radius for the specimen with a

Fig. 5 Comparison of experimental results with Finite Fracture Mechanics prediction. Dashed lines indicate the mean value of experimental results. Solid lines render the numerical results
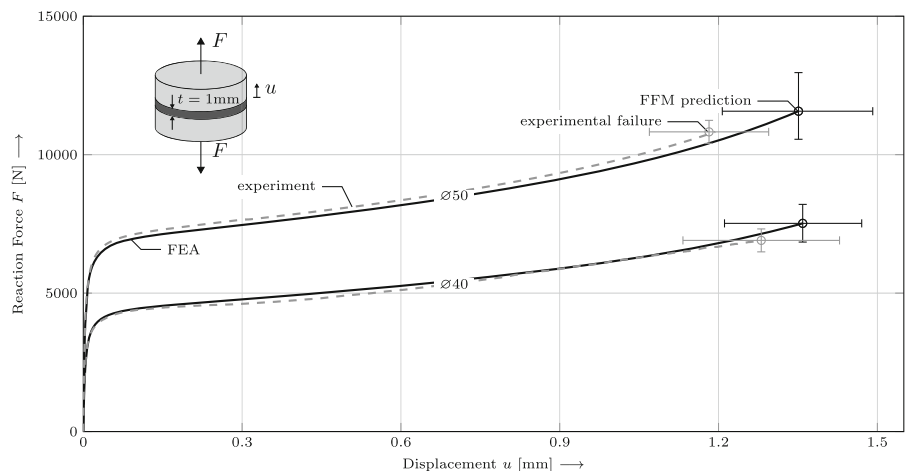
diameter of 50 mm. For these specimens, Santarsiero et al. (2017) reported initial failure at 20 % of the radius. While the failure in the experiments is reported to initiate in the bulk material at the above described distance from the outer edge, the initial failure of the present model does not reach the same region with its finite sized crack. A possible explanation for this deviation is the combination of the applied line method in combination with the non-monotonic stretch distribution along the bi-material interface. The case of a non-monotonic stretch or strength criterion was extensively studied in Talmon l'Armée and Becker (2020). The above study showed, that FFM allows for the creation of internal cracks in certain configuration if the point method is applied. These internal cracks can than be extended to the boundary by the line method. This failure mechanism is assessable with high numerical costs, as all intermediate crack propagation states have to be solved for in the FE-programme. The application of the proposed PMLM-method is therefore considered out-of-scope by the authors for the present study, especially, as the determined fracture loads align well with experimental data.

Additionally, introducing radially symmetric cracks along the entire perimeter of the adhesive layer may result in lower energy release rates compared to asymmetric cracks that nucleate from only one point along the perimeter or within in the material. . Higher incremental energy release rates could occur due to the smaller crack area created. However, analysis of asymmetric cracked penny-shaped bonds is numerically expensive and requires assumptions about the shape of the cracks created. In addition, possible defects in the bond between the adhesive and the adherend are neglected in the numerical analysis. Nevertheless, the results of FFM allow one to study the failure mechanisms present in a closed theoretical framework without making initial assumptions about intrinsic length scales.

Bearing the overestimation of failure loads in mind, this allows for further investigation of the failure behavior of the adhesives . For this purpose, numerical models with different diameters are set up according to Sect. 3. The diameter varies between 10 and 160 mm. Figures 6 and 7 show the results of the FFM predictions as a function of the varying diameter. Figure 7 shows the critical loads in terms of axial displacements, while Fig. 6 shows the critical reaction forces for different diameters. Additionally, Fig. 8 shows the initial crack
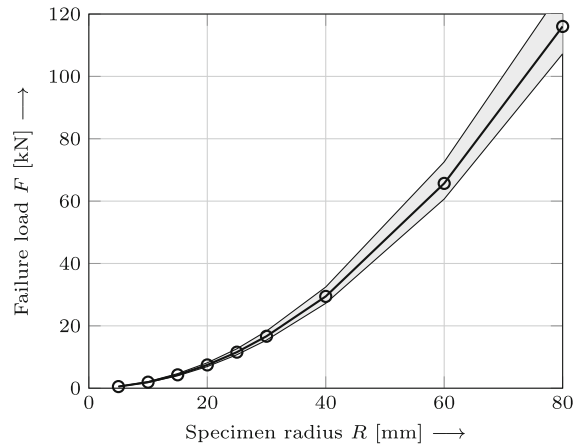

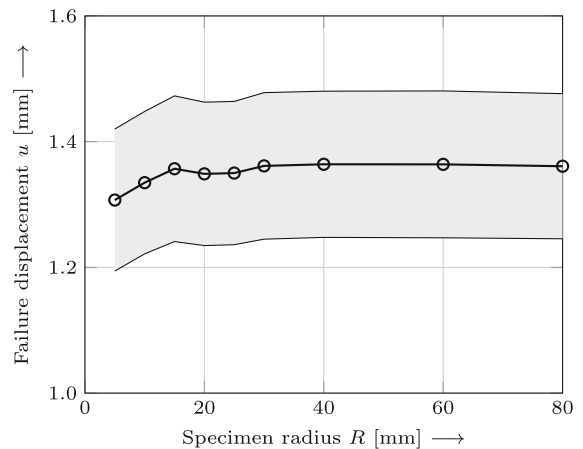**Fig. 6** Failure reaction forces predicted by FFM for varying diameters of the adhesive layer

Fig. 7 Failure displacements predicted by FFM for varying diameters of the adhesive layer
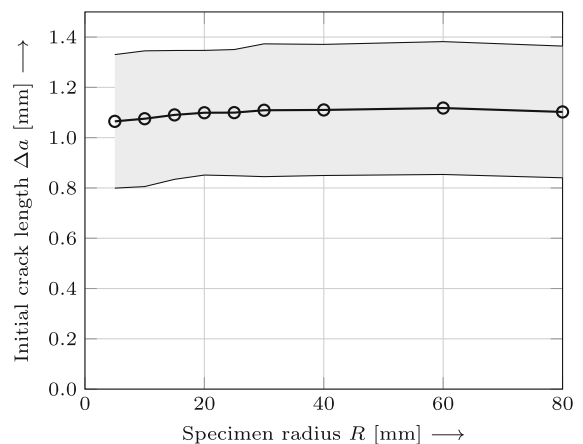

Fig. 8 Predicted initial crack length by FFM for varying diameters of the adhesive layer
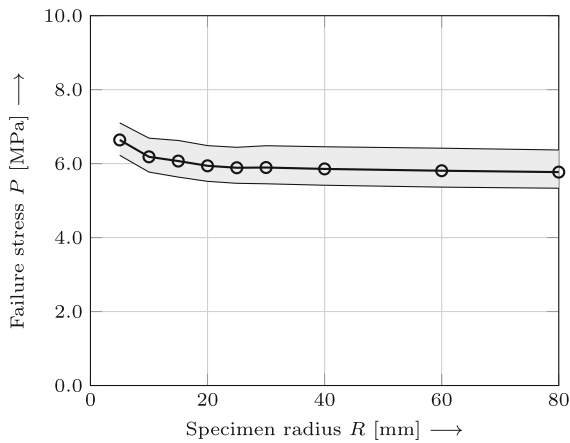
Fig. 9 Failure Piola stresses predicted by FFM for varying diameters of the adhesive layer

lengths, which are an additional solution of the optimization problem.

Figure 7 indicates a plateau in the critical displacements that an adhesive layer can withstand for a wide range of diameters. Smaller diameters generally result in slightly decreasing external displacements. Figure 6 shows the critical reaction forces for different diameters. For better comparison, Fig. 9 shows the area–normalized reaction forces in terms of the critical Piola-Kirchhoff stress. A critical threshold in normal stresses can be observed. For small diameters a slight increase in critical Piola stresses can be noted. This is generally in good agreement with other studies (Bažant 1999; Rosendahl et al. 2018) where small specimens show higher failure loads. Figure 8 shows constant initial crack lengths.

These results can be used to derive engineering models for both initial designs and proofs of strength can be derived. Initial designs can use the Piola-Kirchhoff stress as the nominal tensile strength TSSA fasteners. Detailed proofs of strength are derived from the calculated initial crack lengths. These are the results of a physical sound model for hyperelastic materials, so they can take the role of critical distances proposed by Taylor (2008). According to this approach, an adequate choice of critical crack lengths prevents the fulfillment of the energy criterion and thus the nucleation of an initial crack. This results in a single calculation of the uncracked configuration and the evaluation of the averaged equivalent stretch criterion Eq. 20 at a fixed distance based on the results shown in Fig. 8. Considering the overestimation of the ultimate loads,

sufficient safety factors still need to be considered. In addition, viscous effects have to be considered with different models and further experiments. Nevertheless, the results greatly extend the application range of TSSA, mainly because current industry standards treat hyperelastic adhesives with linear elastic material properties and consider these simplifications with high safety factors. In particular, the onset of cavitation is usually forbidden by normative approaches and critical stresses and stretches are derived from the bifurcation point. This approach leaves a large part of the material's potential load bearing capacity unused, cf. Fig. 5, and explicitly forbids the design of thin adhesive layers for the increased risk of cavitation due to the high lateral constraints when put under axial loading.

5 Conclusion

This study presents the results of applying Finite Fracture Mechanics to thin structural silicone adhesives. Recently developed material models that account for cavitation occurring under strong constraints in thin adhesive layers are used along with current equivalent failure models for silicone materials. The onset of cavitation and subsequent softening of the material should not be taken for a sign of ultimate failure of the material. Rather, the present material model allows to account for the elastic instability that leads to cavitation and can adequately describe the softening. Ultimate failure of the adhesive bonds occurs shortly after the displacement has been greatly increased and an increase in stiffness can be observed. Ignoring this softening and stating that the material fails with the onset of cavitation greatly reduces the regime of applicability of this material and leaves much of the potential of the adhesive untapped.

As observed in other studies, the current results slightly overestimate the experimental results. Although this error is not to be considered on as safe, the results of this study can be used to calibrate engineering models for the design and proof of strength of silicone adhesive DOWSIL™ TSSA . In addition, the method used here is applicable to all silicone adhesives, so that material can be used more efficiently. The high experimental effort required to adequately describe the constitutive behavior of a material and to determine of its equivalent failure surface must be considered a disadvantage. However, the results of this study lead to simpler design

and proof of strength tools for engineers without high numerical or experimental effort in the later use of this material.

In order to improve the predictions of the current model, additional experiments with different geometries and loading specimens are proposed to validate the initial crack length for different configurations. Shear loaded adhesive layers are of particular interest. However, studies on other silicone adhesives show a similar behavior in terms of initial crack lengths. Therefore, the approach taken in this study is considered to be applicable to other silicones and adhesives as well and should be considered as a first approach to more efficient use of building materials in the next generation of technical approval guidelines and industry standards.

Declarations

Conflict of interest The authors have no financial or proprietary interests in any material discussed in this article.

Generative AI and AI-assisted technologies During the preparation of this work the author used DeepL Write in order to improve the readability of the manuscript. After using this tool, the authors reviewed and edited the content as needed and take full responsibility for the content of the publication.

References

Altenbach H, Rosendahl PL, Becker W, Kolupaev VA (2018) Isogonal and isotoxal hexagons as extremal yield figures. In Wisniewski W, Burczynski T (Eds.), Book of abstracts

Arruda EM, Boyce MC (1993) A three-dimensional constitutive model for the large stretch behavior of rubber elastic materi-als. J Mech Phys Solids 41(2):389–412. https://doi.org/10.1016/0022-5096(93)90013-6

Ayatollahi MR, Heydari-Meybodi M, Dehghany M, Berto F (2016) A new criterion for rupture assessment of rubber-like materials under mode-i crack loading: The effective stretch criterion. Adv Eng Mater 18(8):1364–1370. https://doi.org/10.1002/adem.201600046

Ball JM (1982) Discontinuous equilibrium solutions and cavitation in nonlinear elasticity. Philosophical Trans R Soc London Ser A, Math Phys Sci 306(1496):557–611. https://doi.org/10.1098/rsta.1982.0095

Bažant ZP (1999) Size effect on structural strength: a review. Arch Appl Mech 69(9–10):703–725. https://doi.org/10.1007/s004190050252

Berto F (2015) A criterion based on the local strain energy density for the fracture assessment of cracked and v-notched components made of incompressible hyperelastic materials. Theor Appl Fract Mech 76:17–26. https://doi.org/10.1016/j.tafmec.2014.12.008

Blatz PJ (1963) Application of finite elastic theory to the behavior of rubberlike materials. Rubber Chem Technol 36(5):1459–1496. https://doi.org/10.5254/1.3539651

Busse WF (1938) Physics of rubber as related to the automobile. J Appl Phys 9(7):438–451. https://doi.org/10.1063/1.1710439

Cornetti P, Muñoz-Reja M, Sapora A, Carpinteri A (2019) Finite fracture mechanics and cohesive crack model: Weight functions vs. cohesive laws. Int J Solids Struct 156–157:126–136. https://doi.org/10.1016/j.ijsolstr.2018.08.003

Dal H, Cansız B, Miehe C (2018) A three-scale compressible microsphere model for hyperelastic materials. Int J Numer Methods Eng 116(6):412–433. https://doi.org/10.1002/nme.5930

Dal H, Cansız B., Miehe C (2013) Finite element modelisation of multiaxial mechanical and fatigue behavior of a polychloroprene rubber, In *Constitutive Models for Rubber VIII*, eds. Gil-Negrete, N., A. Alonso, 189–194. CRC Press. https://doi.org/10.1201/b14964-35

Danielsson M, Parks D, Boyce M (2004) Constitutive modeling of porous hyperelastic materials. Mech Mater 36(4):347–358. https://doi.org/10.1016/S0167-6636(03)00064-4

Dickie RA, Smith, TL (1969) Ultimate tensile properties of elastomers. vi. strength and extensibility of a styrene–butadiene rubber vulcanizate in equal biaxial tension. J Polymer Sci Part A-2: Polymer Phys 7(4): 687–707. https://doi.org/10.1002/pol.1969.160070408

Doitrand A, Leguillon D (2018) 3d application of the coupled criterion to crack initiation prediction in epoxy/aluminum specimens under four point bending. Int J Solids Struct 143:175–182. https://doi.org/10.1016/j.ijsolstr.2018.03.005

Drass M, Kolupaev VA, Schneider J, Kolling S (2018a) On cavitation in transparent structural silicone adhesive: Tssa. Glass Struct Eng 3(2):237–256. https://doi.org/10.1007/s40940-018-0061-1

Drass M, Schneider J, Kolling S (2018b) Novel volumetric helmholtz free energy function accounting for isotropic cavitation at finite strains. Mater Design 138:71–89. https://doi.org/10.1016/j.matdes.2017.10.059

Drass M, Schwind G, Schneider J, Kolling S (2018c) Adhesive connections in glass structures-part i: experiments and ana-

lytics on thin structural silicone. Glass Struct Eng 3(1):39–54. https://doi.org/10.1007/s40940-017-0046-5

Drass M, Muth J, Louter C, Schneider J (2019) Stress whitening effects in transparent structural silicone adhesives. Glass Struct Eng 4(3):433–448. https://doi.org/10.1007/s40940-019-00102-9

Drass M, Bartels N, Schneider J, Klein D (2020) Pseudo-elastic cavitation model-part ii: extension to cyclic behavior of transparent silicone adhesives. Glass Struct Eng 5(1):67–82. https://doi.org/10.1007/s40940-019-00103-8

Drass M, Du Bois PA, Schneider J, Kolling S (2020) Pseudo-elastic cavitation model: part i-finite element analyses on thin silicone adhesives in façades. Glass Struct Eng 5(1):41–65. https://doi.org/10.1007/s40940-019-00115-4

Drass M, Schneider J (2016) On the mechanical behavior of transparent structural silicone adhesive (tssa), In Zingoni A (ed.). Insights and Innovations in Structural Engineering, Mechanics and Computation. 446–451. Taylor & Francis Group, 6000 Broken Sound Parkway NW, Suite 300, Boca Raton, FL 33487-2742: CRC Press. https://doi.org/10.1201/9781315641645-74

Ehlers W, Eipper G (1998) The simple tension problem at large volumetric strains computed from finite hyperelastic material laws. Acta Mech 130(1–2):17–27. https://doi.org/10.1007/bf01187040

Felger J, Stein N, Becker W (2017) Asymptotic finite fracture mechanics solution for crack onset at elliptical holes in composite plates of finite-width. Eng Fract Mechan 182:621–634. https://doi.org/10.1016/j.engfracmech.2017.05.048

Felger J, Stein N, Becker W (2017) Mixed-mode fracture in open-hole composite plates of finite-width: An asymptotic coupled stress and energy approach. Int J Solids Struct 122–123:14–24. https://doi.org/10.1016/j.ijsolstr.2017.05.039

Felger J, Stein N, Frey C, Becker W (2019) Scaling laws for the adhesive composite butt joint strength derived by finite fracture mechanics. Composite Struct 208:546–556. https://doi.org/10.1016/j.compstruct.2018.09.100

Flory PJ (1961) Thermodynamic relations for high elastic materials. Trans Faraday Soc 57:829. https://doi.org/10.1039/TF9615700829

Frey C, Dölling S, Becker W (2021) Closed-form analysis of interlaminar crack initiation in angle-ply laminates. Composite Struct 257:113060. https://doi.org/10.1016/j.compstruct.2020.113060

García IG, Mantič V, Blázquez A (2018) The effect of residual thermal stresses on transverse cracking in cross-ply laminates: an application of the coupled criterion of the finite fracture mechanics. Int J Fract Mech 211(1–2):61–74. https://doi.org/10.1007/s10704-018-0276-9

García IG, Justo J, Simon A, Mantič V (2019) Experimental study of the size effect on transverse cracking in cross-ply laminates and comparison with the main theoretical models. Mech Mater 128:24–37. https://doi.org/10.1016/j.mechmat.2018.09.006

Gent AN, Lindley PB (1959). Internal rupture of bonded rubber cylinders in tension. Proc R Soc London Ser A Math Phys Sci 249(1257): 195–205. https://doi.org/10.1098/rspa.1959.0016

Griffith AA (1921) Vi. the phenomena of rupture and flow in solids. Philos Trans R Soc London Ser A Math Phys Sci 221(582-593): 163–198. https://doi.org/10.1098/rsta.1921.0006

Hagl A, Wolf A, Sitte S (2012) Investigation of stress-whitening in transparent structural silicone adhesive. In: Bos F, Louter C, Nijsse R, Veer F (eds) Challenging glass 3. IOS Press, Amsterdam, pp 249–258

Hagl A, Dietrich O, Wolf A, Sitte S (2012) Tensile loading of silicone point supports – revisited, In Bos F, Louter C, Nijsse R, Veer F (eds.) Challenging glass 3, Volume 0, 235–247. Amsterdam: IOS Press. https://doi.org/10.3233/978-1-61499-061-1-235

Hamdi A, Mahjoubi H (2015) Design criterion for rubbery parts under biaxial loading. Theor Appl Fract Mech 78:51–55. https://doi.org/10.1016/j.tafmec.2015.04.001

Hamdi A, Naït Abdelaziz M, Aït Hocine N, Heuillet P, Benseddiq N (2006) A fracture criterion of rubber-like materials under plane stress conditions. Polymer Test 25(8):994–1005. https://doi.org/10.1016/j.polymertesting.2006.06.005

Hamdi A, Naït Abdelaziz M, Aït Hocine N, Heuillet P, Benseddiq N (2007) A new generalized fracture criterion of elastomers under quasi-static plane stress loadings. Polymer Test 26(7):896–902. https://doi.org/10.1016/j.polymertesting.2007.06.014

Hashin Z (1996) Finite thermoelastic fracture criterion with application to laminate cracking analysis. J Mech Phys Solids 44(7):1129–1145. https://doi.org/10.1016/0022-5096(95)00080-1

Heydari-Meybodi M, Ayatollahi MR, Dehghany M, Berto F (2017) Mixed-mode (i/ii) failure assessment of rubber materials using the effective stretch criterion. Theo Appl Fract Mech 91:126–133. https://doi.org/10.1016/j.tafmec.2017.05.001

Heydari-Meybodi M, Ayatollahi MR, Berto F (2018) Rupture analysis of rubber in the presence of a sharp v-shape notch under pure mode-i loading. Int J Mech Sci 146–147:405–415. https://doi.org/10.1016/j.ijmecsci.2018.08.008

Horgan CO, Abeyaratne R (1986) A bifurcation problem for a compressible nonlinearly elastic medium: growth of a micro-void. J Elast 16(2):189–200. https://doi.org/10.1007/BF00043585

Hou HS, Abeyaratne R (1992) Cavitation in elastic and elastic-plastic solids. J Mech Phys Solids 40(3):571–592. https://doi.org/10.1016/0022-5096(92)80004-A

Jones TM, Kruse RB (1966) Failure behavior of composite hydrocarbon fuel binder propellants. J Spacecraft Rockets 3(2):265–267. https://doi.org/10.2514/3.28431

Kawabata S (1973) Fracture and mechanical behavior of rubber-like polymers under finite deformation in biaxial stress field. J Macromol Sci Part B 8(3–4):605–630. https://doi.org/10.1080/00222347308201639

Knauss WG (1967) An upper bound of failure in viscoelastic materials subjected to multiaxial stress states. Int J Fract Mech 3(4):267–277. https://doi.org/10.1007/BF00182892

Kolupaev VA (2018) Equivalent stress concept for limit state analysis, Volume 86 of Advanced Structured Materials. Cham: Springer International Publishing

Lake GJ, Thomas AG (1967) The strength of highly elastic materials. Proc R Soc London Ser A Math Phys Sci 300(1460):108–119. https://doi.org/10.1098/rspa.1967.0160

Lake GJ (1995) Fatigue and fracture of elastomers. Rubber Chem Technol 68(3):435–460. https://doi.org/10.5254/1.3538750

Lazopoulos KA, Ogden RW (1998) Nonlinear elasticity theory with discontinuous internal variables. Math Mech Solids 3(1):29–51. https://doi.org/10.1177/108128659800300103

Leguillon D (2002) Strength or toughness? a criterion for crack onset at a notch. Eur J Mech A/Solids 21(1):61–72. https://doi.org/10.1016/S0997-7538(01)01184-6

Leguillon D, Martin E, Ševeček O, Bermejo R (2015) Application of the coupled stress-energy criterion to predict the fracture behaviour of layered ceramics designed with internal compressive stresses. Eur J Mech A/Solids 54:94–104. https://doi.org/10.1016/j.euromechsol.2015.06.008

Leguillon D, Martin E, Ševeček O, Bermejo R (2018) What is the tensile strength of a ceramic to be used in numerical models for predicting crack initiation? Int J Fract Mech 212(1):89–103. https://doi.org/10.1007/s10704-018-0294-7

Li J, Mayau D, Song F (2007) A constitutive model for cavitation and cavity growth in rubber-like materials under arbitrary tri-axial loading. Int J Solids Struct 44(18–19):6080–6100. https://doi.org/10.1016/j.ijsolstr.2007.02.016

Li J, Mayau D, Lagarrigue V (2008) A constitutive model dealing with damage due to cavity growth and the mullins effect in rubber-like materials under triaxial loading. J Mech Phys Solids 56(3):953–973. https://doi.org/10.1016/j.jmps.2007.06.009

Lindsey GH (1967) Triaxial fracture studies. J Appl Phys 38(12):4843–4852. https://doi.org/10.1063/1.1709232

Lopez-Pamies O, Idiart MI, Nakamura T (2011a) Cavitation in elastomeric solids: I-a defect-growth theory. J Mech Phys Solids 59(8):1464–1487. https://doi.org/10.1016/j.jmps.2011.04.015

Lopez-Pamies O, Nakamura T, Idiart MI (2011b) Cavitation in elastomeric solids: Ii-onset-of-cavitation surfaces for neo-hookean materials. J Mech Phys Solids 59(8):1488–1505. https://doi.org/10.1016/j.jmps.2011.04.016

Miehe C, Schänzel LM (2014) Phase field modeling of fracture in rubbery polymers. part i: Finite elasticity coupled with brittle failure. J Mech Phys Solids 65:93–113. https://doi.org/10.1016/j.jmps.2013.06.007

Mooney M (1940) A theory of large elastic deformation. J Appl Phys 11(9):582–592. https://doi.org/10.1063/1.1712836

Nelder JA (1966) Inverse polynomials, a useful group of multi-factor response functions. Biometrics 22(1):128. https://doi.org/10.2307/2528220

Ogden RW (1972) Large deformation isotropic elasticity – on the correlation of theory and experiment for incompressible rubberlike solids. Proc R Soc London Ser A Math Phys Sci 326(1567): 565–584. https://doi.org/10.1098/rspa.1972.0026

Pipes RB, Wetherhold RC, Gillespie JW (1979) Notched strength of composite materials. J Comp Mater 13(2):148–160. https://doi.org/10.1177/002199837901300206

Podgórski J (1985) General failure criterion for isotropic media. J Eng Mech 111(2):188–201. https://doi.org/10.1061/(ASCE)0733-9399(1985)111:2(188)

Rheinschmidt F, Schneider J, Rosendahl PL (2023) Identification of mode i and iii fracture toughness of hyperelastic adhesives. J Adhes Adhes (under review)

Rivlin RS (1948) Large elastic deformations of isotropic materials iv. further developments of the general theory. Philos Trans R Soc London Ser A Math Phys Sci 241(835): 379–397. https://doi.org/10.1098/rsta.1948.0024

Rivlin RS, Thomas, AG (1953) Rupture of rubber. i. characteristic energy for tearing. J Polymer Sci 10(3): 291–318. https://doi.org/10.1002/pol.1953.120100303

Rosendahl PL, Drass M, Schneider J, Becker, W (2018) Crack nucleation in hyperelastic adhesive bonds. ce/papers 2(5-6):409–425. https://doi.org/10.1002/cepa.941

Rosendahl PL, Weißgraeber P (2020) Modeling snow slab avalanches caused by weak-layer failure - part 1: Slabs on compliant and collapsible weak layers. Cryosphere 14(1):115–130. https://doi.org/10.5194/tc-14-115-2020

Rosendahl PL, Weißgraeber P (2020) Modeling snow slab avalanches caused by weak-layer failure - part 2: Coupled mixed-mode criterion for skier-triggered anticracks. Cryosphere 14(1):131–145. https://doi.org/10.5194/tc-14-131-2020

Rosendahl PL, Weißgraeber P, Stein N, Becker W (2017) Asymmetric crack onset at open-holes under tensile and in-plane bending loading. Int J Solids Struct 113–114:10–23. https://doi.org/10.1016/j.ijsolstr.2016.09.011

Rosendahl PL, Drass M, Felger J, Schneider J, Becker W (2019) Equivalent strain failure criterion for multiaxially loaded incompressible hyperelastic elastomers. Int J Solids Struct 166:32–46. https://doi.org/10.1016/j.ijsolstr.2019.01.030

Rosendahl PL, Staudt Y, Schneider AP, Schneider J, Becker W (2019) Nonlinear elastic finite fracture mechanics: Modeling mixed-mode crack nucleation in structural glazing silicone sealants. Mater Design 182:108057. https://doi.org/10.1016/j.matdes.2019.108057

Santarsiero M, Louter C, Nussbaumer A (2017) Laminated connections under tensile load at different temperatures and strain rates. Int J Adhes Adhes 79:23–49. https://doi.org/10.1016/j.ijadhadh.2017.09.002

Sharma MG (1966) Failure of polymeric materials under biaxial stress fields. Polymer Eng Sci 6(1):30–35. https://doi.org/10.1002/pen.760060106

Sharma MG, Lim CK (1965) Experimental investigations on fracture of polymers. Polymer Eng Sci 5(4):254–262. https://doi.org/10.1002/pen.760050408

Sitte S, Brasseur MJ, Carbary LD, Wolf AT, Wolf A, Dean SW (2011) Preliminary evaluation of the mechanical properties and durability of transparent structural silicone adhesive (tssa) for point fixing in glazing. J ASTM Int 8(10):104084. https://doi.org/10.1520/JAI104084

Smith TL, Rinde JA (1969) Ultimate tensile properties of elastomers. v. rupture in constrained biaxial tensions. J Polymer Sci Part A-2: Polymer Phys 7(4):675–685. https://doi.org/10.1002/pol.1969.160070407

Souguir S, Brochard L, Sab K (2020) Stress concentration and instabilities in the atomistic process of brittle failure initiation. Int J Fract Mech 224(2):235–249. https://doi.org/10.1007/s10704-020-00459-x

Staudt Y, Odenbreit C, Schneider J (2018) Failure behaviour of silicone adhesive in bonded connections with simple geometry. Int J Adhes Adhes 82:126–138. https://doi.org/10.1016/j.ijadhadh.2017.12.015

Stein N, Weißgraeber P, Becker W (2015) A model for brittle failure in adhesive lap joints of arbitrary joint configuration.

Composite Struct 133:707–718. https://doi.org/10.1016/j.compstruct.2015.07.100

Stuart CA (1985) Radially symmetric cavitation for hyperelastic materials. Ann Inst Henri Poincaré C, Anal Non Linéaire 2(1):33–66. https://doi.org/10.1016/S0294-1449(16)30411-5

Talmon l'Armée A, Becker W (2020) Coupled stress and energy criterion for composite failure: Pointwise versus averaged evaluation of the stress criterion. Mechan Adv Mater Struct 27(18):1571–1582. https://doi.org/10.1080/15376494.2018.1519618

Talmon A, Hell S, Rosendahl PL, Felger J, Becker W (2017) Nonlinear crack opening integral: Mode mixity for finite cracks. Eng Fract Mechan 186:283–299. https://doi.org/10.1016/j.engfracmech.2017.10.006

Taylor D (2008) The theory of critical distances. Eng Fract Mech 75(7):1696–1705. https://doi.org/10.1016/j.engfracmech.2007.04.007

Thomas AG (1955) Rupture of rubber. ii. the strain concentration at an incision. J Polymer Sci 18(88):177–188. https://doi.org/10.1002/pol.1955.120188802

Thomas AG (1958) Rupture of rubber. v. cut growth in natural rubber vulcanizates. J Polymer Sci 31(123): 467–480. https://doi.org/10.1002/pol.1958.1203112324

Timmel M, Kaliske M, Kolling S, Mueller R (2007) A micromechanical approach to simulate rubberlike materials with damage. Comput Mater Continua 5(3):161–172. https://doi.org/10.3970/cmc.2007.005.161

Tschoegl NW (1971) Failure surfaces in principal stress space. J Polymer Sci Part C: Polymer Symp 32(1):239–267. https://doi.org/10.1002/polc.5070320113

Weißgraeber P, Felger J, Geipel D, Becker W (2016) Cracks at elliptical holes: Stress intensity factor and finite fracture mechanics solution. Eur J Mech A/Solids 55:192–198. https://doi.org/10.1016/j.euromechsol.2015.09.002

Weißgraeber P, Leguillon D, Becker W (2016) A review of finite fracture mechanics: crack initiation at singular and non-singular stress raisers. Arch Appl Mech 86(1–2):375–401. https://doi.org/10.1007/s00419-015-1091-7

Yerzley FL (1939) Adhesion of neoprene to metal. Indust Eng Chem 31(8):950–956. https://doi.org/10.1021/ie50356a007